Simulations of flow over a bio-inspired undulated cylinder with dynamically morphing topography

Mikihisa Yuasa[1], Kathleen Lyons[2], Jennifer A. Franck[3,*]

Department of Engineering Physics, University of Wisconsin-Madison, Madison, WI

Abstract

Inspired by the geometric properties of seal whiskers, the addition of spanwise undulations on a cylinder have been shown to lower the mean and oscillatory forces and modify the frequency of flow-induced vibration when compared to smooth cylinders. Previously, computational fluid dynamics (CFD) has been used to characterize the hydrodynamic response with respect to specific geometric features. However simulations are time intensive due to complex three-dimensional meshing and computation time, limiting the number of geometric perturbations explored. A method is proposed in which the specific geometric features of this complex topography can be modified during a simulation thereby decreasing the time per geometric modification and removing the need for manual meshing of the complex structure. The surface of the seal whisker inspired geometry is parameterized into seven defining parameters, each of which is directly controlled in order to morph the surface into any realization within the defined parameter space. Once validated, the algorithm is used to explore the undulation amplitudes in the chord and thickness directions, by varying each independently from 0 to 0.3 thicknesses in increments of 0.05 at a Reynolds number of 500. The force and frequency response are examined for this matrix of geometric parameters, yielding detailed force trends not previously investigated. The impact of the bio-inspired morphing algorithm will allow for further optimization and development of force-mitigating underwater devices and other engineering applications in need of vibration suppression, frequency tuning, or force reduction.

Keywords: fluid-structure interaction, vortex-induced vibrations, seal whiskers, drag reduction, dynamic meshing, bio-inspired fluid dynamics

*Corresponding author
Email address: jafranck@wisc.edu (Jennifer A. Franck)
[1]Undergraduate Research Assistant
[2]Graduate Research Assistant
[3]Assistant Professor

1. Introduction

Inspired by the unique geometry of seal whiskers, this paper computationally investigates the fluid flow over an undulated cylinder by actively morphing the geometry. Unlike other mammals, seals have bumps along the span of the whiskers, forming a unique undulated cylindrical geometry [1]. Undulated cylinders that mimic the flow response of seal whiskers have been shown to reduce drag and vortex-induced vibrations (VIV) by modifying the coherent wake structures typical of smooth cylinders [2].

The force reduction properties of undulated cylinders create intriguing design options for various engineering systems, such as hydrodynamic sensors, towing cables, support structures, and aerodynamic components. However, the fluid flow response of the complete set of undulated topographies has not yet been thoroughly characterized due to the large number of geometric parameters and potential flow regimes. Testing many geometric iterations is time-consuming as the spanwise undulations and subsequent variations in cross-section impose challenges to consistent and high-quality surface rendering and mesh generation for computational investigations. This research proposes an analytical definition of the bio-inspired undulated cylinder surface geometry and a dynamic meshing routine to actively morph the surface to a sequence of prescribed topographies during a flow simulation.

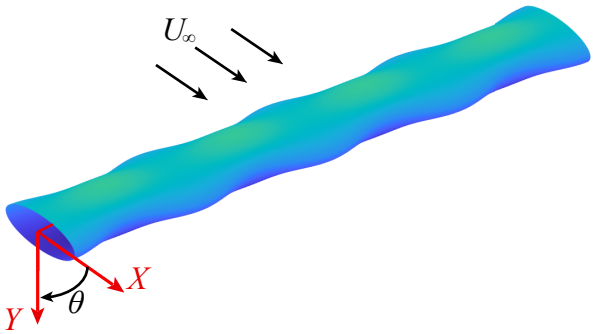

(a) Isometric view of a seal whisker inspired undulated cylinder.

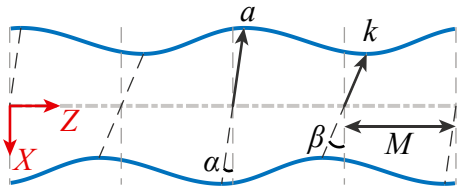

(b) Geometric parameters, xz-plane.

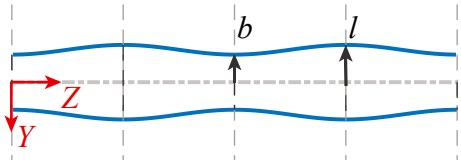

(c) Geometric parameters, yz-plane.

Figure 1: Isometric and cross-sectional views of undulated cylinder geometry, as defined by Hanke et al. [2]. Flow is in the positive x-direction.

The first seal whisker model geometry was described by Hanke et al. [2], who used digital photography measurements of 13 harbor seal whiskers to create seven geometric parameters that describe the spanwise periodic geometry. The model geometry contains two sets of spanwise undulations out of phase with one another as shown in Figure 1. Two inclined ellipses, described by their minor and major axes and the inclinations angles in the $x-z$ plane, form the interior structure of the model along with the half-wavelength distance M. Using this model in a combination of simulations and experiments, Hanke et al. confirmed that the the flow over the undulated structure did not display the regular pattern of alternating shed vortices typical of smooth topographies and the von Kármán vortex street was replaced with a higher pressure and more symmetric wake, effectively eliminating VIV.

The dual undulation geometric model described by Hanke et al. has been commonly used in fluid flow studies around the undulated cylinder [3–7] . Building on work by Ginter et al [8] and Murphy [9], an independent investigation characterized mean geometric parameters from 27 whiskers, including both harbor and elephant seals [10]. This work presented a wide statistical variability in whisker geometry, confirmed by morphological analyses showing geometric variation within and between species [1]. There have been a handful of investigations that explore the influence of geometric variation such as comparing two distinct wavelengths [3], removing one set of undulations [4], or shifting the phase between two sets of undulations [11].

Recent work by Lyons et al. redefined the seven geometric parameters of the whisker model with respect to hydrodynamic relevance and explored a low and high perturbation from each nondimensional parameter from a baseline geometry [6]. A matrix of 16 geometric parameter combinations was created and a large-eddy simulation (LES) was used to assess the effect of each parameter on the overall flow response. The parameters that most significantly affect the flow response were found to be the aspect ratio, the wavelength, and the two undulation amplitudes.

Each of the previous computational investigations has been limited in the number of distinct models explored, making it difficult to assess the impacts of individual geometric parameters. Simulations are time intensive due to the three-dimensional geometry and inherent time-dependent and unsteady flow phenomena that must be resolved. Computational time is driven by the resolution and small time-step requirements, but there is also a large time investment for the manual mesh generation of each new three-dimensional geometry proposed, including debugging for mesh errors and a long transient time to reach steady state before time-averaged statistics can be collected.

Furthermore, the nominal model of Hanke et al. [2], widely used in most experimental and numerical investigations, does not explicitly define the surface geometry for the entire whisker model. As defined, the end user must interpolate the smooth surface topography between the two defining ellipses at the peak and trough locations. This ill-defined interpolation process introduces geometric variability from model to model

and inevitably creates mild discrepancies in the measured flow response across various investigations.

To alleviate the computational limitations and variability among geometric models, the current paper introduces a morphing whisker defined by the first complete topographic parameterization of the whisker surface. The analytic surface description is incorporated into a dynamic mesh morphing algorithm such that the geometric undulations are prescribed by the user throughout a single simulation, and the computational flow solver responds immediately to the changes in topography.

Using the newly developed method, the two orthogonal undulation amplitudes of the seal whisker model are modified systematically. Previous work has identified amplitude as an important parameter for drag reduction response [6, 12], and that the combination of two amplitudes in orthogonal directions is more beneficial than just one set of undulations [4, 7]. Recent research has also indicated that there may be a broad range of wavelengths and amplitudes at which the mean and fluctuating forces are reduced, perhaps beyond the morphological values found in seal whiskers [11]. To explore the amplitude parameter space in more detail, the undulated geometry is modified with the dynamic surface morphing technique. In the same manner as Lyons et al. [6], the two undulation amplitudes are recast into a nondimensional and hydrodynamically relevant chord length amplitude and thickness amplitude, allowing for one amplitude to be varied independent of another while holding the wavelength and phase-bias parameters constant. The results produce a matrix of seven chord length amplitudes by seven thickness amplitudes, for a total of 49 distinct undulated cylinder geometries. The flow response in terms of mean and fluctuating forces is discussed, linking it to the formation of unsteady flow structures and corresponding frequency spectra.

The algorithm and computational details are described in detail in Section 2. Section 3 compares the newly developed topography with previous results and documents the transient response of the flow to the mesh morphing process. Finally, the flow response to changes in two orthogonal undulation amplitudes is presented, highlighting changes to the forces, flow structures, and frequency spectra as a function of each undulation amplitude.

2. Methods

2.1. Overview of Surface Morphing Strategy

Staten et al. detail the surface morphing process for newly formed three-dimensional shapes encompassing a vast variation of geometries and outline the general process as follows: define the final surface node positions, the curves connecting the nodes, and finally the surface mesh [13]. In a survey of techniques, Samreh et al. describe the various categories of mesh deformation, summarizing the advantages and disadvantages of each approach [14]. The method described in this paper falls under the basis vector approach, in which an analytical expression for the surface is developed and the changes from the initial to final state are

prescribed by a sequence of vectors. The basis vector approach for dynamic meshing maintains the underlying structure of the surface mesh, which is beneficial for computational fluid dynamics (CFD) as it satisfies several requirements for fast simulation and convenient post-processing [15]. These benefits include the ability to consistently deform the target shape smoothly regardless of the complexity, utilize the minimum number of geometric variables to describe shape variations, maintain compatibility with existing geometries, and maintain stability of the solution. An example of the basis vector approach is implemented by Wei et al., who detail the motion of a structured mesh surface variation of square building corners, accomplished by moving mesh points in a single direction [16].

Taking a similar approach to Wei et al., the sequence of vectors describing the nodal motion of the undulated cylinder surface are confined to the radial direction, as illustrated in Figure 2. For simplicity, the original undeformed geometry is depicted as a smooth cylinder without any undulations in Figure 2a. However in practice, this initial geometry can be more complex and contain undulations defined by the prescribed analytical expressions. The underlying structured surface mesh contains N_z points across the span and N_θ points around the circumference. A vector, $\mathbf{r}_o$, defined from the z-axis, describes the location of each surface point. For the simple case of a smooth cylinder, the vector $\mathbf{r}_o$ is a constant radius.

The final undulated cylinder in Figure 2b is defined to be spanwise periodic (along the z-axis) and each xy-plane maintains its z-coordinate throughout the morphing. Thus, points are constrained to move radially within the xy-plane throughout the deformation. The vector defining the final location of the deformed mesh point is given by $\mathbf{r}_f$, and the transformation vector is the difference between the final and initial shape. To ensure a smooth transition and stability of the fluid flow solver, the deformation is specified by multiple intermediate shapes by dividing the transformation vector into a sequence of vectors $\Delta\mathbf{r}_i$ [17], giving an expression for the final location as

$$\mathbf{r}_f = \mathbf{r}_o + \sum_i \Delta\mathbf{r}_i. \tag{1}$$

Moving the points radially ensures they maintain the same θ and z position before and after deformation. Thus, parameterization of the three-dimensional geometry is performed by examining the surface at each unique θ, as depicted in the xz-plane of Figure 2c. In this view, the surface geometry can be described as having a radius r, which is a function of z and the fixed parameter θ, or $r(z;\theta)$.

2.2. Parameterization of the Undulated Cylinder Surface

Hanke et al. first characterized the whisker morphology by seven topographic parameters as shown in Figure 1: four semi-axes of the two inclined cross-sectional ellipses (a, b, k, l), two angles that define the ellipse inclination (α, β), and one distance parameter between the two ellipses (M) [2]. This definition contains inclined cross-sectional ellipses within the whisker geometry, only a skeletal structure of the geometry. Thus

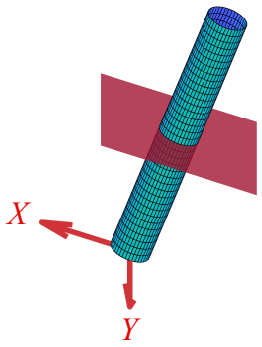

(a) Initial mesh surface

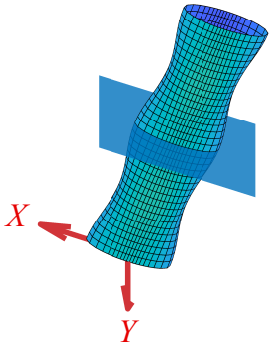

(b) Final mesh surface

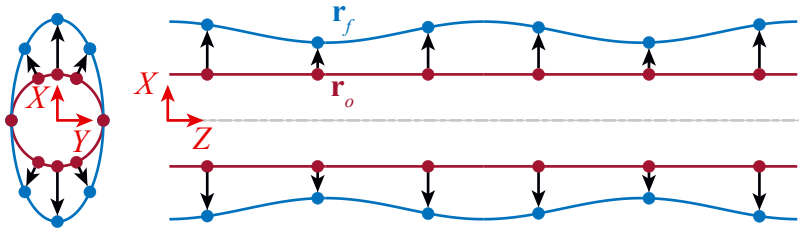

(c) Transition of surface mesh points from initial to final state

Figure 2: Overview of the surface mesh morphing from the initial to the final geometry based on the basis vector approach in which the surface points are confined to motion in the radial direction.

a complete analytical expression for the surface remains undefined. In order to morph the surface nodes into a new undulated geometry, the function $r(z;\theta)$ connecting the inclined ellipses must be defined with respect to the seven geometric parameters of the inclined ellipses.

The parameterized function for $r(z;\theta)$ is a two-part piecewise cosine function that intersects the geometry defining ellipses at points R_1 and R_2, as shown in Figure 3. As the geometry is rotated about the z-axis (thus changing the parameter θ), the radial and spanwise location of R_1 and R_2 move, but they remain the extrema of the function $r(z;\theta)$ by definition.

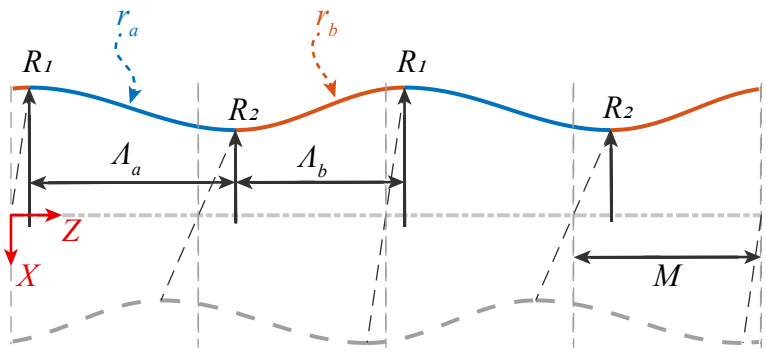

Figure 3: Schematic of the surface parameterization.

The radii R_1 and R_2 are calculated as

$$R_1 = \frac{ab\cos\alpha}{\sqrt{(a\cos\alpha\sin\theta)^2 + (b\cos\theta)^2}} \tag{2}$$

$$R_2 = \frac{kl\cos\beta}{\sqrt{(k\cos\beta\sin\theta)^2 + (l\cos\theta)^2}} \tag{3}$$

using the original ellipse parameters with a detailed derivation in Appendix Appendix A.1. The wavelengths of the cosine functions, Λ_a and Λ_b, are similarly computed for each θ position as

$$\Lambda_a \equiv M - R_1\cos\theta\tan\alpha + R_2\cos\theta\tan\beta \tag{4}$$

$$\Lambda_b \equiv M + R_1\cos\theta\tan\alpha - R_2\cos\theta\tan\beta \tag{5}$$

and are a function of R_1 and R_2, as well as the original ellipse parameters. Finally, the piecewise surface characterization function is expressed as

$$r(z;\theta) = \begin{cases} r_{a,n} \equiv \frac{R_1-R_2}{2}\cos(\frac{\pi}{\Lambda_a}(z - z_{1,n})) + \frac{R_1+R_2}{2} & \text{if } \; z_{1,n} \le z < z_{2,n} \\ r_{b,n} \equiv -\frac{R_1-R_2}{2}\cos(\frac{\pi}{\Lambda_b}(z - z_{2,n})) + \frac{R_1+R_2}{2} & \text{if } \; z_{2,n} \le z < z_{1,n+1} \end{cases} \tag{6}$$

where

$$z_{1,n} \equiv -R_1 \cos\theta \tan\alpha + 2nM$$
$$z_{2,n} \equiv -R_2 \cos\theta \tan\beta + M + 2nM$$

and $n \in \mathbb{N}$.

Therefore, the surface vector $\mathbf{r}$ is expressed as $\mathbf{r}(r(z;\theta),\theta,z)$. The derivation above completes the analytical expression of the undulated whisker surface geometry based on the seven parameters that define the skeleton.

To morph between an initial and final geometry, a transformation vector is defined as $\mathbf{r} \equiv \mathbf{r}_f - \mathbf{r}_o$. Over a prescribed transformation time period, the surface experiences a smooth transition from the initial shape to the final shape using a time-dependent sigmoid function $\varsigma(t)$, scaled so that the transformation completes within the user-defined prescribed time period yielding

$$\mathbf{r}_f = \mathbf{r}_o + \varsigma(t)\mathbf{r} \quad \text{where} \quad 0 \leq \varsigma(t) \leq 1. \tag{7}$$

The smooth and gradual transition from the initial to the final shape described by Equation (7) is illustrated in Figure 4.

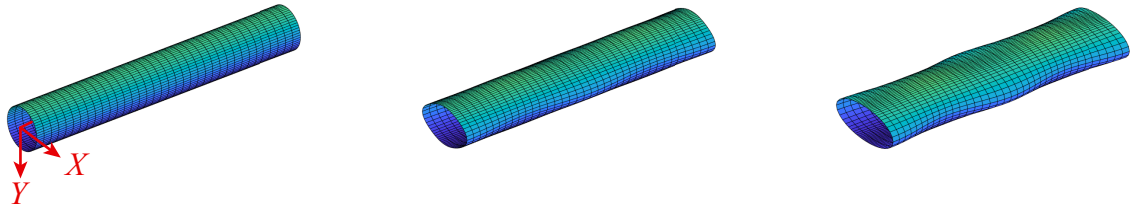

(a) The initial cylinder; $\varsigma = 0$ (b) An intermediate topography (c) The final cylinder; $\varsigma = 1$

Figure 4: Transformation process using a time-dependent sigmoid function.

2.3. Computational Details

The computational scheme utilizes the *OpenFOAM* finite volume libraries [18] to compute the flow field and the mesh motion resulting from the the morphing whisker geometry. The governing equations for the fluid flow are the incompressible Navier-Stokes equations,

$$\frac{\partial}{\partial t}\mathbf{u} = -\frac{1}{\rho}\nabla p - (\nabla \cdot \mathbf{u})\mathbf{u} + \nu\nabla^2\mathbf{u} \tag{8}$$

$$\nabla \cdot \mathbf{u} = 0 \tag{9}$$

where $\mathbf{u}$ is the velocity vector, ρ is the density, p is the pressure, and ν is the kinematic viscosity. The surface morphing described in Section 2.2 initiates the mesh motion of all computational cells in the domain. To account for the mesh motion of each cell, an additional equation is solved at every timestep to update the mesh nodal displacement field, $\mathbf{x_m}$, at every point in the computational domain. The nodal displacement is governed by the mesh motion equation

$$2\nabla \cdot [\mu \nabla \mathbf{x_m}] + \nabla \cdot [\mu((\nabla \mathbf{x_m})^T - \nabla \mathbf{x_m} - \mathbf{I}\,\mathrm{tr}(\nabla \mathbf{x_m}))] = 0, \tag{10}$$

which is known as the solid body rotation (SBR) stress equation [19]. Once the mesh has been updated, the fluid solver updates the velocity and pressure based on the new mesh coordinates and the volume flux imposed by the mesh motion. The variable μ represents a diffusivity in the mesh motion and is inversely proportional to the distance from the mesh node to the cylinder surface. This setup ensures that the motion of the cells is spread out over the entire domain and not contained to the local deformation of the surface. Consequently, the mesh resolution near the surface, and thus within the boundary layer, does not change drastically as the cylinder evolves from one undulated topography to the next.

The dynamic mesh motion is driven through the boundary conditions at the surface of the cylinder, which are prescribed according to the equations presented in Section 2.2. As shown in Figure 5, the outer boundary is prescribed zero motion and remains stationary. During the morphing process, the mean thickness, T, of the cylinder remains constant, and is subsequently used as a reference length. The computational domain is circular in the xy-plane with a radius of $75T$ and extends two wavelengths in the spanwise direction, L_z. Inlet flow boundary conditions are prescribed for $x < 0$, whereas outlet flow conditions are prescribed for $x > 0$, and periodic boundary conditions are applied across the span. A second-order finite volume method is utilized within *OpenFOAM* with a standard pressure-implicit split-operators (PISO) solver, and a second-order backward scheme is used to advance time.

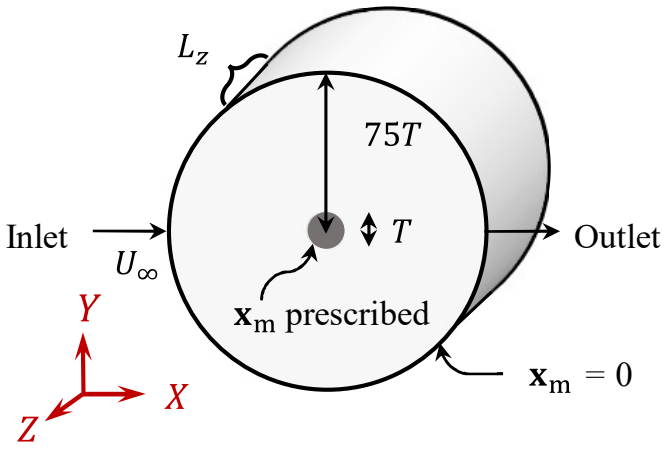

Figure 5: Schematic of the initial 3D computational domain with a smooth cylinder at center.

2.4. Simulation Parameters and Workflow

Fluid flow simulations are performed at an angle of attack of zero degrees such that the flow aligns with the x-axis, perpendicular to the cylinder thickness. The Reynolds number of the simulations is $Re_T = 500$, nondimensionalized by the mean thickness, T. As shown by Figure 6, the amplitude of the undulations are defined by A_C, the amplitude in the chord or streamwise direction, and A_T, the amplitude in the thickness or transverse direction. Both amplitudes are normalized by the mean thickness, T. Defining the amplitudes in this manner allows for each amplitude to be varied independently of one another while holding other hydrodynamically relevant parameters constant, such as the wavelength and aspect ratio. Changing the amplitudes A_T and A_C requires modification of six of the original geometric parameters, as $A_T = |b - l|/T$ and $A_C = |a\cos\alpha - k\cos\beta|/T$. A thorough explanation of the relationship between the amplitude-based geometric parameters of Figure 6 and the ellipse-based geometric parameters of Figure 1 can be found in Lyons et al. [6].

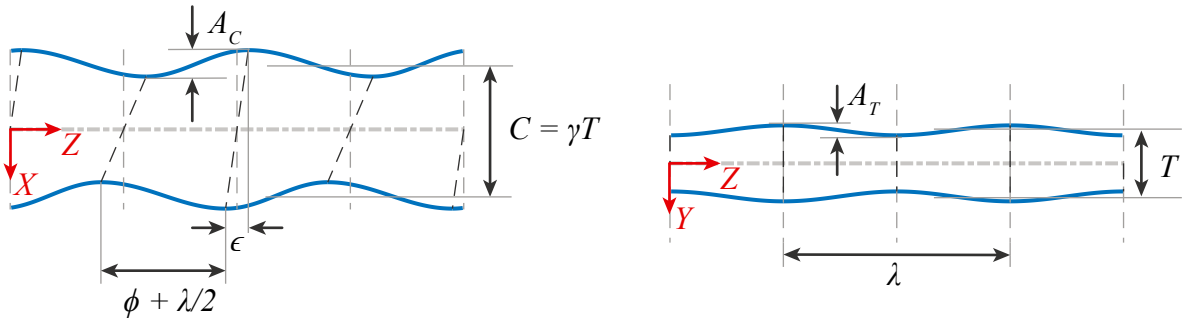

Figure 6: Geometric definitions of the amplitude in the chord length A_C, amplitude in the thickness A_T, the wavelength λ, aspect ratio γ, and the asymmetry parameters ϵ and ϕ.

The wavelength λ, nondimensionalized by thickness T, is 3.43, and the aspect ratio γ, the ratio of the mean chord length to mean thickness, is 1.92. The remaining two nondimensional quantities that introduce asymmetry into the model's undulations as seen in whisker specimens are also held constant at $\epsilon = 0.342$ and $\phi = 0.015$. These values match the geometric parameters in the nominal model by Hanke et al [2], and are similar to values utilized in previous studies [3, 4, 6, 7]. To investigate the effect that changes in amplitude have on the flow response, each of the two nondimensional amplitudes is varied independently from 0 to 0.3 in increments of 0.05 while all other geometric parameters remain constant.

After each variation in geometry, the flow is allowed time to adjust to steady state conditions after which the flow response is averaged to compute the mean drag coefficient $\overline{C_D}$, the root-mean-square (RMS) value of the lift oscillations $C_{L,RMS}$, and the frequency spectra from the lift oscillations. The drag and lift coefficients C_D, C_L are computed as

$$C_D = \frac{2F_D}{\rho U_\infty^2 T L_z} \tag{11}$$

$$C_L = \frac{2F_L}{\rho U_\infty^2 C L_z} \tag{12}$$

where U_∞ is the freestream velocity, L_z is the span length in the z-direction, and ρ is the fluid density. The drag and lift forces, F_D and F_L, are normalized by the averaged frontal and planform areas TL_z and CL_z, respectively. The frequency of the oscillating lift f is nondimensionalized as

$$f^* = \frac{fT}{U_\infty}. \tag{13}$$

The dominant peak in the lift spectrum is reported as the Strouhal number, St. Each new geometric perturbation is allotted 10 convective time units (CTU) for the transition, 150 CTU for the transient flow response once the shape has been formed and another 450 CTU for the steady state to collect the values of response variables.

Figure 7 compares the proposed mesh morphing workflow (red) and a standard manual meshing workflow (blue) while iterating through multiple geometric models. The major advantage of the proposed mesh morphing workflow is the human input is removed from the iteration process, converting the manual hours of mesh generation and debugging to CPU hours. Thus, dynamic mesh morphing can be implemented during an active simulation to transform the model from one topography into the next without user intervention. The proposed method also decreases simulation time due to the faster transient regimes, as transitioning from one geometry with fully-developed flow to another geometry with fully developed flow is computationally faster than transitioning from an initial condition of uniform flow at all cells. Finally, the initial input of the user can be a very simple mesh, in this case a two-dimensional (extruded) circular cylinder, which is easy to create, refine, and validate.

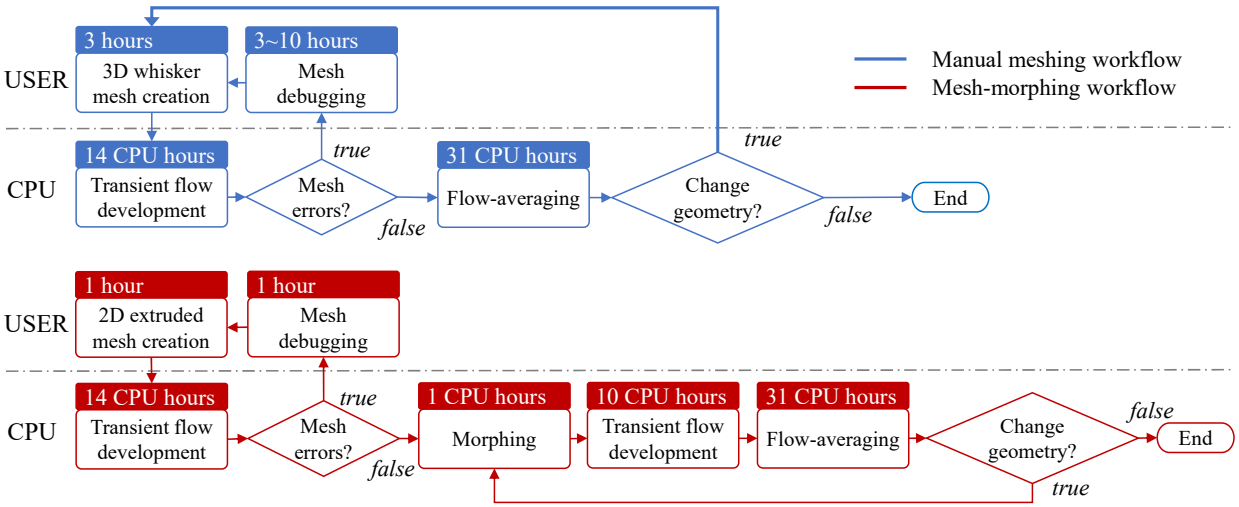

Figure 7: Comparison between a traditional mesh-solve-repeat process for iterating through multiple geometric configurations (top, in blue) and the proposed mesh morphing workflow (bottom, in red).

2.5. Mesh Resolution

While the current work investigates a range of amplitude values, mesh independence verification is performed for the widely investigated model geometry presented by Hanke et al. [2], hereafter referred to as the nominal model. For this model, $A_C = 0.23$ and $A_T = 0.09$. The mesh resolution study is performed by creating four smooth cylinder meshes of various resolutions as the initial shape, each morphed into the nominal whisker model geometry. The four initial mesh resolutions are described in Table 1 in terms of the nodes in the radial, circumferential, and spanwise directions. Mesh points are clustered around the surface of the cylinder in the radial direction for resolution of the boundary layer (BL), clustered around the cylinder wake in the circumferential direction, and evenly spaced in the spanwise direction.

Table 1: Resolution and mesh attributes of the underlying cylinder (initial configuration).

Number of total mesh nodes N	2.57M	1.92M	1.39M	0.718M
N_z	110	100	90	68
N_θ	216	196	176	160
N_r	110	100	90	68
Mesh points in BL at $\theta = 90^\circ$	17	16	15	12
$\Delta\theta_{\min}$	0.009561	0.01129	0.01331	0.01550
$\Delta\theta_{\max}/\Delta\theta_{\min}$	3.137	2.678	2.254	1.935

Each simulation progresses to a fully developed flow over the initial circular cylinder geometry before initiating the surface morphing algorithm. The hydrodynamic forces $(\overline{C_D}, C_{L,rms})$ resulting from each of the four different mesh resolutions in Table 1 are compared with one another and with those of previous investigations in Table 2. As the resolution is increased, the mean drag slowly decreases to where there is only a 0.9% difference at the added expense of 0.65 million cells between the two most refined meshes, whereas the RMS lift force fluctuates between 0.0099 and 0.0122. The four mesh resolutions have comparable results with the previous studies at $Re_T = 390 - 500$ despite the small changes in undulated geometry that exist from model to model, due to no common surface definition. These changes are demonstrated in more detail in Section 3.1. Based on these results, and to best conserve the computational time, the mesh resolution of 1.92M is selected to carry out the current simulations.

Table 2: Mesh configurations of the undulated cylinder model compared with previous literature. Reynolds number from previous literature converted to be based on mean thickness, T, for consistency.

	N	Re_T	$\overline{C_D}$	$C_{L,RMS}$
0.718M	0.718M	500	0.741	0.0157
1.39M	1.39M	500	0.714	0.0129
1.92M	1.92M	500	0.708	0.0099
2.57M	2.57M	500	0.701	0.0122
Lyons et al. [6]	1.92M	500	0.717	0.0111
Lyons et al. [6]	0.718M	500	0.715	0.0163
Witte et al. [3]	8M	390	0.769	0.0173
Hans et al. [4]	N/A	390	N/A	0.011
Kim and Yoon [20]	3.5M	390	0.741	0.0167

3. Results

3.1. Validation of Surface and Mesh Morphing

The method described in Section 2.2 is, to the best of the authors' knowledge, the first analytical parameterization of the entire seal whisker surface. The parameterization utilizes and maintains the definitions of the inclined cross-sectional ellipses first proposed by Hanke et al. [2] and commonly used by researchers, and it also completely describes the periodic surface geometry between the ellipses. To assess the difference between the proposed analytical surface and surfaces created by other techniques, a comparison is performed with the topography in Lyons et al. [6]. In Lyons et al, the model is formed from two sets of inclined ellipses (for two wavelengths) and the whisker surface is created with the computer-aided-design (CAD) software *Solidworks* using a sequence of splines. Both models have the same nominal value of parameters a, b, k, l, M, α and β, although the interpolation between the inclined ellipses is performed differently.

To perform the comparison, the surface mesh from Lyons et al. is used as an initial configuration and the mesh morphing algorithm is subsequently applied. Thus, any radial motion of the mesh points will indicate differences between the new surface parameterization and the CAD generated surface. Figure 8a illustrates the distribution of the radial difference between each mesh point. The comparison shows that 96.6% of the mesh points are within 2% thickness difference with the original location. The maximum difference is 4.07% of the whisker thickness T and the mean and median difference are 0.59% and 0.41%, respectively.

Figure 8b highlights the locations of larger radial coordinate differences across the two wavelengths. The largest differences can be observed near (x, y, z) = (-1, 0, 0.6) as well as (1, 0, 6.868) which is hidden due to the orientation in Figure 8b. The differences in Figure 8b also highlight that although the underlying ellipses form a periodic scaffold in the CAD implementation, this periodicity is not automatically applied in the *Solidworks* spline surface generation, leading to imperfect surface periodicity. The analytic function proposed in this paper alleviates this problem by mathematically describing the entire periodic surface.

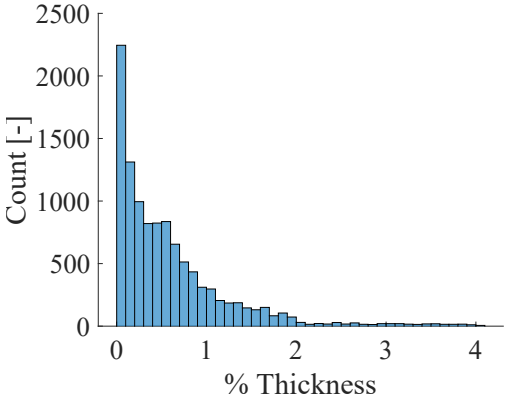

(a) Distribution of coordinate difference in the radial direction.

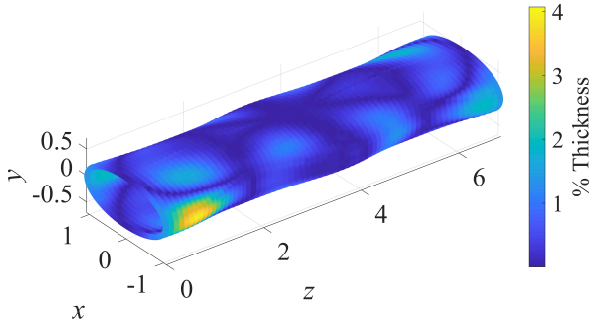

(b) Mesh points of the newly generated surface compared with previous surface generation in Lyons et al. [6]. Colors indicate coordinate displacement in radial direction.

Figure 8: Illustration of (a) distribution and (b) locations of radial coordinate differences between a whisker surface generated by Lyons et al. [6] and by the newly proposed algorithm.

The novelty of the proposed algorithm is in the analytical formation and surface morphing of the seal whisker topology. However, changes in the the surface geometry drive the motion of the entire nodal field in the domain as defined per Equation (10). Thus, Figure 9 displays the mesh properties in the vicinity of the body throughout the morphing from a smooth cylinder into the nominal whisker model. Two spanwise locations are examined on the peak and trough of the thickness undulation. The structured mesh remains structured throughout the evolution of the mesh deformation and the aspect ratio remains relatively stable. The equiangle skewness angle, or the deviation from orthogonal element angles, has a maximum of 0.17 in the original cylinder mesh, increasing to 0.37 along the trough cross-section, both of which are well below the recommended maximum value of 0.5-0.9. Whereas Figure 9 demonstrates typical mesh properties of the results found in this paper, the mesh properties can be further tuned and improved by generating a custom distribution of mesh cells in the initial cylinder geometry, or by modifying the governing mesh deformation equation (Equation (10)) and/or its diffusivity parameter μ.

Finally, the hysteresis of the surface morphing and resulting mesh motion is investigated by morphing a smooth cylinder to a nominal seal whisker model and then back to a smooth cylinder. By examining the

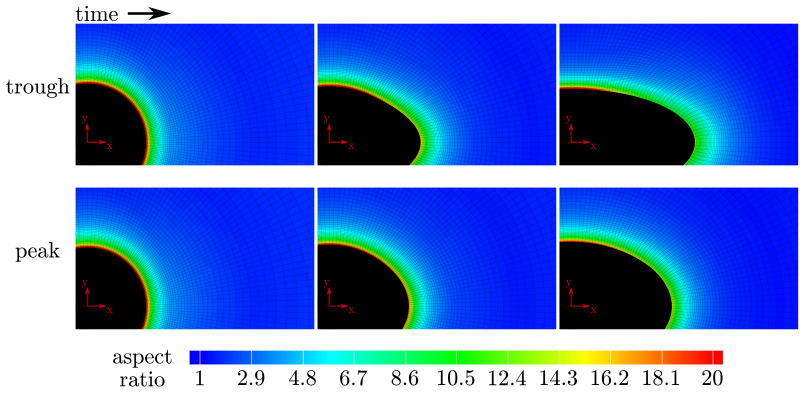

(a) The cell aspect ratio remains similar at both spanwise cross-sections as the mesh changes from a circular cylinder to the nominal seal whisker model.

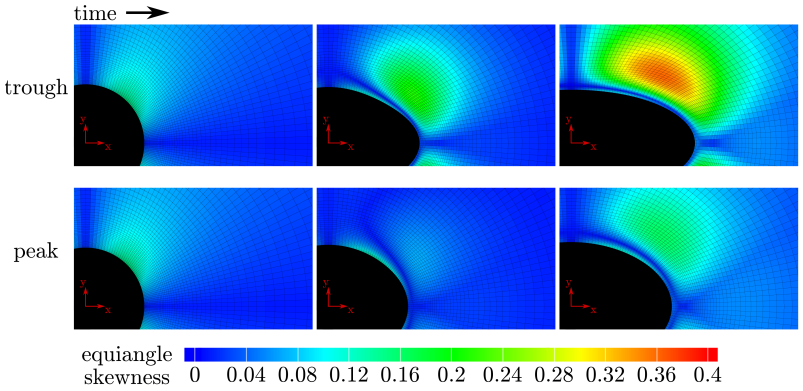

(b) The equiangle skewness is increased from a maximum value of 0.17 to 0.37 in the seal whisker model.

Figure 9: The cell aspect ratio and equiangle skewness mesh metrics are displayed at the thickness peak and trough locations at select times during the morphing. From left to right: circular cylinder mesh, halfway morphed, nominal seal whisker geometry.

displacement of each node in the field at the final timestep, the maximum displacement between the initial and final cylinder mesh is on the order of 1×10^{-10}, which is an order of magnitude smaller than the prescribed tolerance of 1×10^{-9} on the mesh motion solver. This confirms that neither the analytical equations prescribing the motion of the surface mesh nor the resulting mesh motion of the interior computational domain have hysteresis effects. Thus, moving from one intermediate geometry to another will elucidate the same geometric response regardless of the number and path of prescribed morphing iterations.

3.2. Transient Response of the Flow

Although the mesh motion does not create hysteresis, the flow solver and the physical response of the flow take some time to adjust to the modified surface geometry. To investigate the transient flow response, the drag coefficient is examined through the morphing from a steady state cylinder flow to the nominal whisker model and the reverse morphing back into a cylinder. Figure 10 displays the forces for each of these regimes, color coded for steady state (blue), active morphing (red), and transient flow (green). From this data, it is confirmed that the mean steady state forces in the final cylinder flow matches with that of the initial cylinder flow. The transition period is chosen conservatively to be 150 CTUs, however could likely be reduced further based on this data. The morphing is performed over 10 CTUs, which is also chosen conservatively. The drag coefficient from different rates of morphing is shown in the inset of Figure 10, demonstrating that a slower rate (50 CTUs) and a faster rate (5 CTUs) both converge to the same mean drag force before the end of the transient regime.

In a second demonstration of the morphing algorithm, a geometric transformation is performed with four undulated cylinder models where $A_T = 0$ and A_C increases through the values $A_C = 0.0$, 0.1, 0.2, and 0.3, as shown in Figure 11. The hydrodynamic forces are recorded throughout the process, with the same morphing rate (10 CTUs) and transition time (150 CTUs) as Figure 10. From the response seen in both the drag and lift of Figure 11, the flow quickly adapts to new geometries and achieves a new steady state. The steady state regime (shown in blue) is where the time-averaged force statistics are computed.

In a rough estimate of the time savings for this four geometry simulation (using the values in Figure 7) the manual meshing and debugging process is reduced from 24 hours to 2 hours. This savings would only grow if more modifications are added, as there is no additional time cost for remeshing. Both methods take an equal amount of CPU time for four geometries, however the mesh-morphing becomes slightly more efficient as the number of geometries increase. This savings could be improved with less conservative transient flow times, which may be suitable for various applications.

3.3. Influence of Amplitude on Forces

To explore the effects of geometric modifications to a whisker inspired undulated cylinder, the two amplitude parameters are varied independently between 0 and 0.3 while holding the remaining geometric pa-

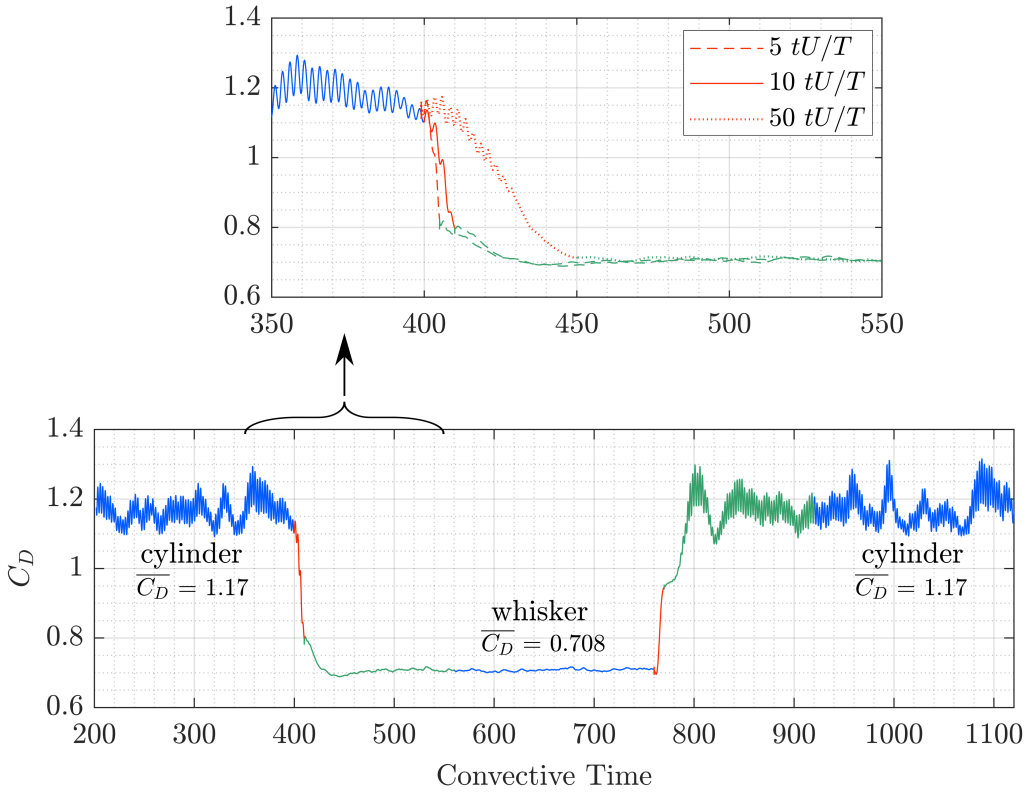

Figure 10: The plot of drag force with respect to time illustrates the same force response for a circular cylinder before and after morphing to the nominal seal whisker model. Blue: steady state regime; Red: active morphing, Green: transient flow. The inset displays three rates of morphing of 50 (slow), 10 (moderate), or 5 (fast) convective time units.

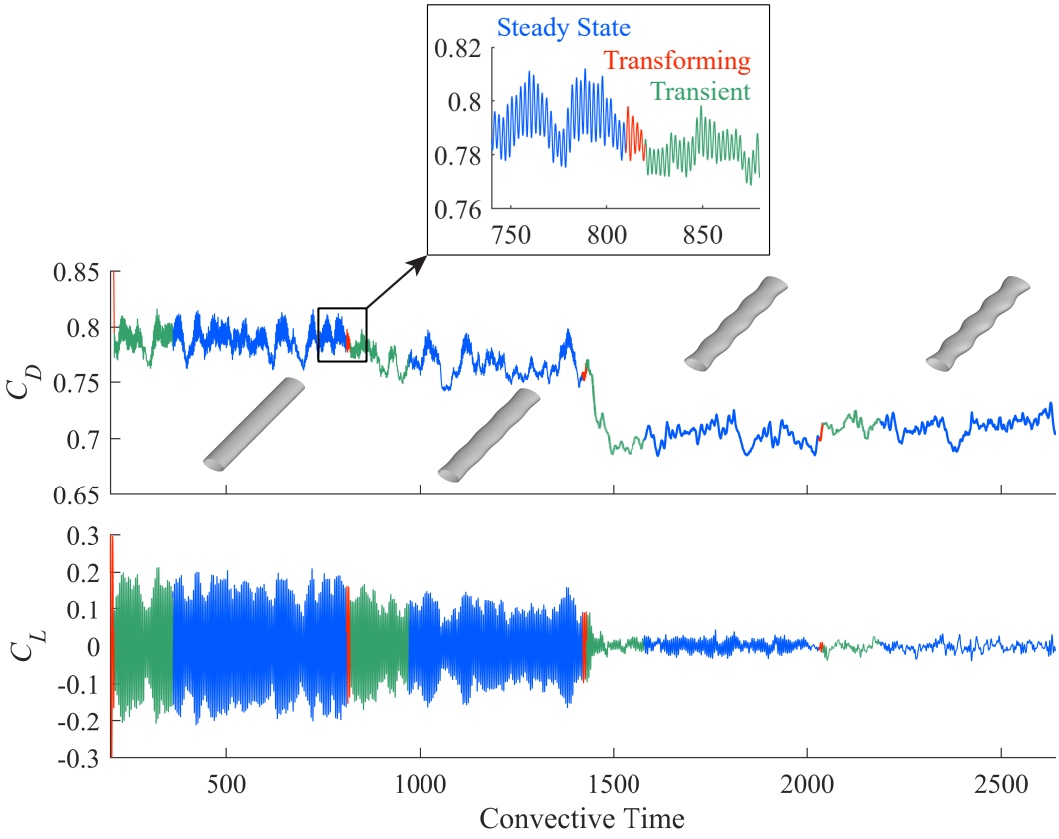

Figure 11: Results from a single simulation including mesh-morphing transitions between four models are shown. Models have a fixed value of $A_T = 0$ with $A_C = 0$, 0.1, 0.2, and 0.3. Plots of drag coefficient (top) and lift coefficient (bottom) show smooth mesh morphing transitions between each of the four geometric models.

rameters constant, forming a matrix of 49 undulated cylinder geometries. The dynamic mesh morphing algorithm is utilized to reduce the 49 geometries to eight simulations, as shown in Figure 12, with each simulation containing six or seven unique topographies.

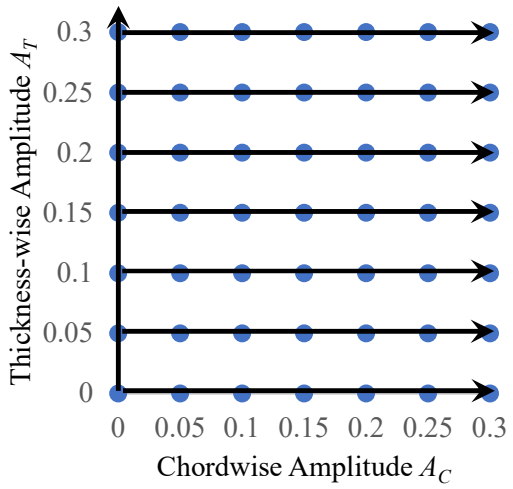

Figure 12: Parameter space of A_C and A_T variation. Each solid line denotes one simulation with multi-step transformations using the mesh morphing algorithm.

The hydrodynamic response for each of the 49 whisker geometries is quantified by $\overline{C_D}$ and $C_{L,RMS}$ with results shown in Figure 13. Both $\overline{C_D}$ and $C_{L,RMS}$ show similar trends with respect to A_C and A_T, with maximum values in the lower left corner where A_T and A_C are zero, indicating the smooth elliptical cylinder topography. When $A_T = 0$, the drag and oscillating lift coefficients decrease slightly as A_C increases from 0 to 0.1. However, a larger drop is seen during the transition from an A_C of 0.1 to 0.2. Similarly when $A_C = 0$, $\overline{C_D}$ and $C_{L,RMS}$ decrease as A_T increases from 0 to 0.3. However, the forces are reduced more quickly with the introduction of A_T than A_C. The response suggests the potential for a limiting threshold value for A_C and A_T if oscillating lift and drag reduction is desirable.

At low to moderate A_T values, $A_T = 0.05$ and 0.1, $C_{L,RMS}$ continues the previous pattern of reduction with increasing A_C. The drag initially decreases as A_C increases with local minima at $(A_C, A_T) = (0.05, 0.1)$ and $(0.15, 0.05)$ then begins to increase again at larger A_C values but remains lower than the absolute maximum at $(0, 0)$. These local $\overline{C_D}$ minima do not align with $C_{L,RMS}$ minima. Therefore, careful selection of geometric parameters should be made in order to achieve the desired response based on application. When $A_T \geq 0.15$, $\overline{C_D}$ generally monotonically increases with larger A_C values; however, the $C_{L,RMS}$ response is more complex. For $A_T \geq 0.1$, the local minima occur when $A_C = 0.05 - 0.1$. Finally when $A_T = 0.3$, $C_{L,RMS}$ is consistently low from $A_C = 0 - 0.15$, giving a wider region of low lift oscillations in the top left

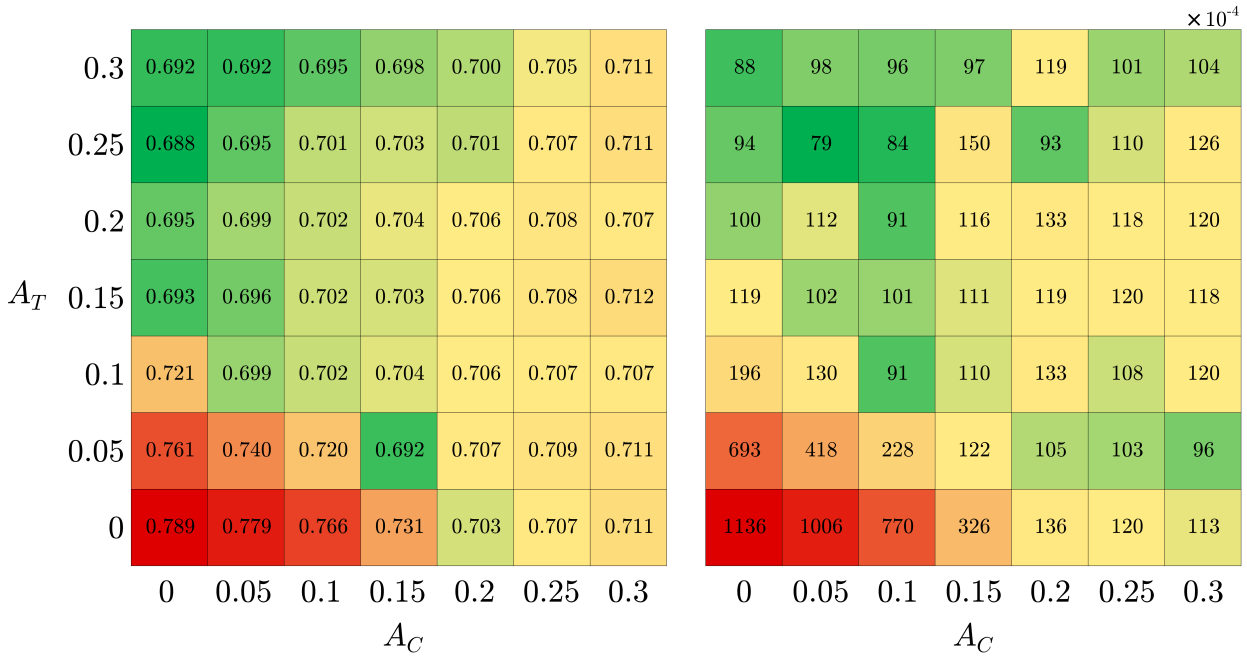

Figure 13: Flow response in terms of $\overline{C_D}$ (left) and $C_{L,RMS}$ (right) for the 49 geometric variations of amplitudes.

corner, and a global minimum at $(A_C, A_T) = (0.05, 0.25)$.

Although it is clear that small changes in A_T and A_C affect the flow, the dominant effects are examined by looking at flow features from the extreme values, $(A_C, A_T) = (0, 0.3)$, $(0.3, 0)$ and $(0.3, 0.3)$. Given the changes in spanwise undulations across the models, notable differences can be seen in the spanwise velocity component, U_z. Figure 14a displays the spanwise velocity of the these three cases within two yz-planes, one near the leading edge and another just before the trailing edge of the geometry. In the $(0, 0.3)$ case, there are large undulations in thickness and thus the freestream flow is quickly redirected into the positive and negative z-direction to overcome the change in thickness, displaying strong (10% of freestream) spanwise velocity immediately at the leading edge. Flow also continues to accelerate in the streamwise direction as shown by the streamlines in Figure 14b. The early onset of the spanwise velocity component gives way to alternate bands of transverse vorticity forming at the leading edge and continuing to grow along the surface before being transported into the wake as seen in Figure 14c. Interestingly, the spanwise velocity is lower at the trailing edge than the leading edge. Of the three cases demonstrated, this has the lowest mean drag and the lowest RMS lift.

In the second column is $(A_C, A_T) = (0.3, 0)$, corresponding to a large amplitude in the chord and no undulations in thickness. In contrast to the first model, the $(0.3, 0)$ geometry produces a minimal amount

of spanwise velocity at its leading edge. Spanwise flow develops as it travels over the surface, and has increased substantially by the trailing edge, revealing large regions of alternating positive and negative flow with $U_z > 0.1U_\infty$. This later development of spanwise velocity is a consequence of the spanwise pressure gradient induced by the change in local chord length. As flow moves over the shorter chord length cross-sections, a larger adverse pressure gradient is created than for the more streamlined (long chord length) cross-sections. Thus, the flow shifts towards the low pressure region near the long chord length trailing edge as can be visualized by the streamlines in Figure 14b which seem to accumulate around the locations of highest amplitude at the trailing edge. In contrast to the high thickness amplitude model, this process develops very little transverse vorticity along the surface.

In the third column of Figure 14, $(A_C, A_T) = (0.3, 0.3)$ demonstrates a super-positioning of two large amplitudes in both chord and thickness. The initial spanwise velocity is muted due to the presence of the chord length amplitude, and the tendency of the streamlines to gather at the highest chord amplitude is diminished with the introduction of the thickness amplitude. Nevertheless, the $(0.3, 0.3)$ model develops transverse vorticity early and then appears to sustain the layers further downstream as the spanwise flow feeds into them at the trailing edge. This most extreme combination of amplitudes still has a moderate drag reduction compared to other models tested, matching that of the $(0.3, 0)$ model, and a low to moderate RMS lift reduction, performing better than $(0.3, 0)$.

3.4. Influence of Amplitude on Lift Force Frequency

Introduction of three-dimensional vorticity as shown in Figure 14c can help prevent a dominant two-dimensional spanwise shear layer roll-up, a phenomenon previously noted by others [11, 12]. In addition to decreasing the amplitude of the lift response, the changes in vortical shedding patterns directly affect the frequency distribution of the lift signal. An analysis of the lift spectrum provides insight into the flow characteristics of each topography. A single St value may characterize the dominant frequency of some flow patterns. However, comparing the full frequency spectra allows for a better understanding of the subtle flow differences among these models. The lift spectra for select models are shown in Figure 15. Each spectrum plot is paired with isosurfaces of Q-criterion, which visualizes the strength of vortices in the wake and demonstrates the variation in these vortical structures.

The baseline smooth elliptical cylinder, $(A_C, A_T) = (0, 0)$, is shown in the lower left and displays a strong peak in the frequency domain at a reduced frequency of $f^* = 0.22$. This sharp peak is associated with a mostly two-dimensional shedding of alternating sign vorticity typical of smooth cylinders. Moving upwards from the lower left in Figure 15, the dominant amplitude at approximately 0.22 shifts to a slightly lower frequency in $(A_C, A_T) = (0, 0.1)$ before forming lower and broader peaks in $(0, 0.2)$ and $(0, 0.3)$. This dramatic change is associated with a breakup of the spanwise coherent structures shown in the baseline model and consistent with a large decrease in forces shown in Figure 13. The spectrum at $(0, 0.3)$ has a

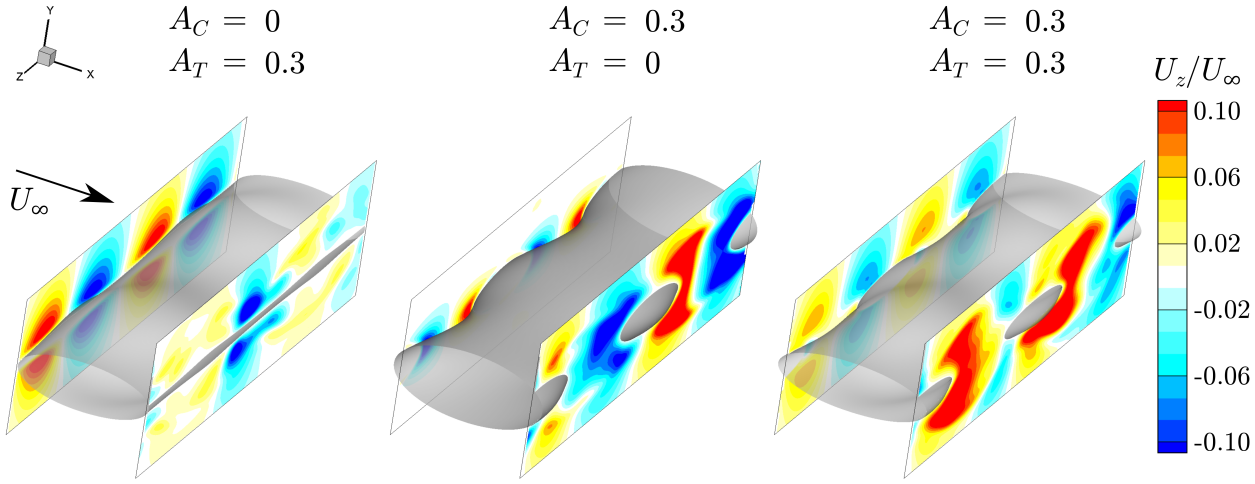

(a) Contours of spanwise velocity at xy-planes near the leading edge and trailing edge

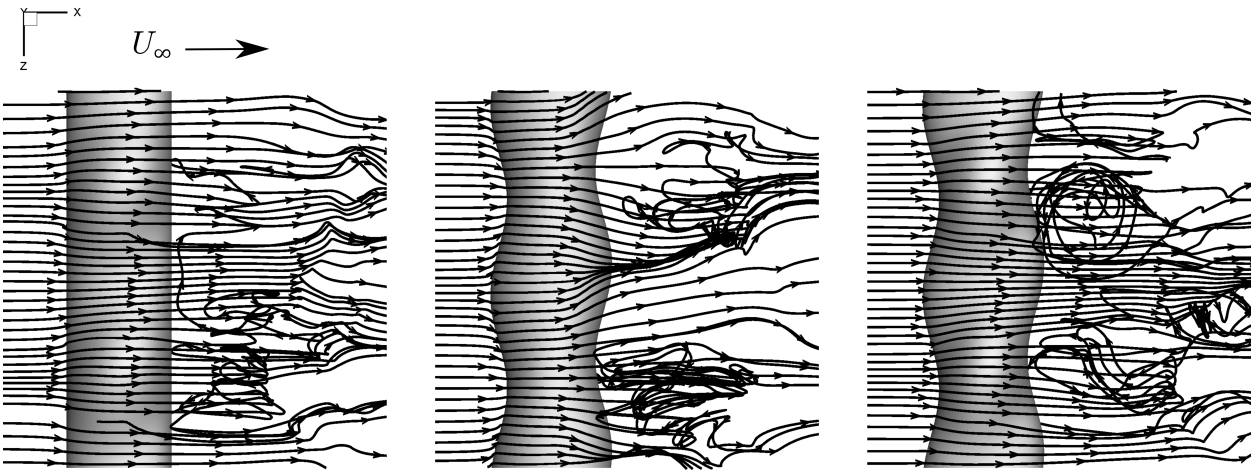

(b) Instantaneous streamlines

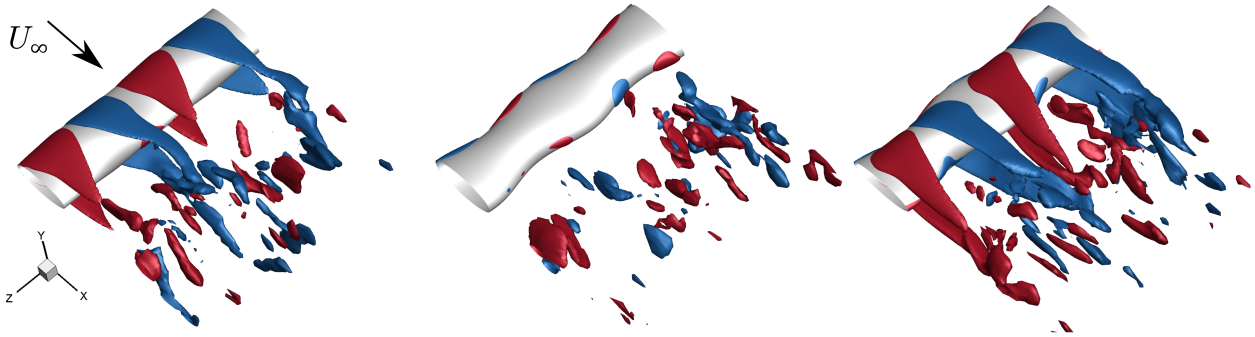

(c) Isosurfaces of transverse vorticity, positive vorticity in red and negative in blue

Figure 14: Comparison among simulated cases with extreme amplitudes, $(A_C, A_T) = (0, 0.3)$, $(0.3, 0)$, and $(0.3, 0.3)$, shows the variation in induced spanwise flow and subsequent transverse vorticity development.

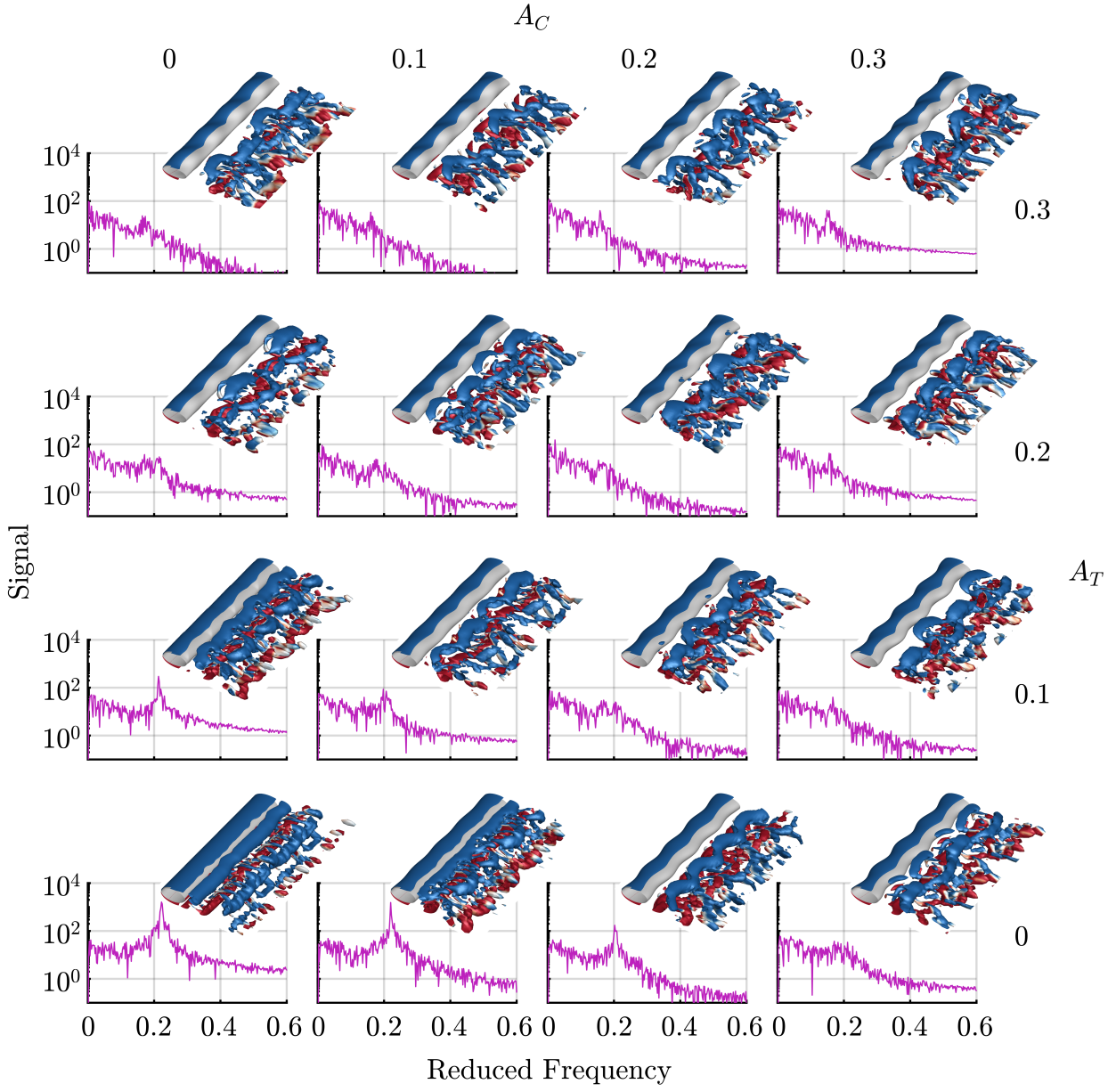

Figure 15: Shedding frequency spectra for a range of cases $A_C = 0, 0.1, 0.2, 0.3$ and $A_T = 0, 0.1, 0.2, 0.3$.

diminished peak at $f^* = 0.16$ with an amplitude approximately two orders of magnitude lower than the dominant peak in the baseline model.

When A_T is held constant and A_C increases (moving from left to right), the peak gradually reduces in amplitude and slightly decreases its frequency. This is most clearly demonstrated in the bottom two rows. At $(A_C, A_T) = (0, 0.1)$ a similar response to the smooth cylinder exists. However it has been replaced with a very broad peak from $f^* = 0.17 - 0.21$ at $(0.2, 0.1)$, and only a small peak at $f^* = 0.17$ remains when $(A_C, A_T) = (0.3, 0.1)$. The isosurfaces are each unique and show decreasing levels of spanwise coherence with smaller spectral amplitudes and frequency shift. The lowest levels of drag and RMS lift are represented across the top left side of Figure 15, where the amplitude of the signal drops off quickly for any frequencies above the peak at $f^* = 0.17$. At the highest A_T amplitude of 0.3 moving from left to right along the top row, there are fewer changes in the spectra as the dominant frequency is $f^* = 0.16$, shifting to $f^* = 0.15$ when $A_C = 0.3$. In this row there is a notable increase in amplitude of the higher frequencies with increasing A_C, which is not likely to be visible in the isosurfaces displayed.

4. Conclusion

A new surface morphing technique is introduced that is able to modify features of the seal whisker model geometry during CFD simulations, creating a faster and simpler mechanism for exploring geometric variations. Using the base geometric scaffold previously defined by two inclined ellipses [2], the complete surface topography is parameterized, which eliminates small changes in surface rendering between various implementations of seal whisker models. To implement the algorithm, a simple two-dimensional extruded cylinder flow can be used as an initial condition, eliminating the many hours of manual meshing and debugging for complex three-dimensional geometries. Despite the time savings in manual meshing, the mesh morphing algorithm does not increase the overall CPU time.

Next, the mesh morphing algorithm is used to explore the two amplitudes of the seal whisker model, one in the chord direction (A_C) and one in the thickness direction (A_T). Large values of both A_C and A_T (up to 30% of the thickness) are shown to increase spanwise transport although through different mechanisms. The creation of spanwise velocity near the leading edge results in the development of transverse vorticity, giving large A_T geometries a slight advantage in force reduction compared with large A_C geometries. The combination of extreme values of A_C and A_T does not provide any further reduction in drag or lift forces. At smaller amplitudes, combinations of undulations work together to increase flow three-dimensionality producing local minima such as the model $(A_C, A_T) = (0.1, 0.1)$. Accordingly, the lift force frequency spectra show broader dominant peaks at lower frequencies for cases with considerable breakup of spanwise flow structures.

The results of the 49 model geometries offer much more detail into the force and flow response as a

function of undulation amplitude but are consistent with data presented in previous work. The effects of the presence of both undulations were assessed in the computational work by Yoon et al. where, building on the work of Hans et al., seven whisker inspired models were simulated and compared with a smooth elliptical cylinder [4, 7]. Yoon et al. concluded that non-zero values of both A_C and A_T are required for maximum reduction of drag and oscillating lift. They also noted that the introduction of A_C had a larger impact on the force reduction than the introduction of A_T [7]. Within the range of A_C and A_T values simulated, $A_C \approx 0.23$ and $A_T \approx 0.09$, the results presented here support both of these conclusions. A wider range of amplitude values was investigated by Lui et al., although both amplitude parameters were modified together to maintain a constant local aspect ratio rather than varying A_C and A_T independently [11]. Their results showed consistent low values of $\overline{C_D}$ and $C_{L,RMS}$ across the range of amplitude values simulated. Lyons et al. simulated only two A_C and two A_T values and reported A_C to have a more significant effect on $\overline{C_D}$ [6]. However in this more detailed exploration, both amplitudes are shown to reduce $\overline{C_D}$ when compared to a smooth elliptical cylinder, albeit through different mechanisms.

This newly proposed mesh transformation algorithm can further enable feature variation within the seal whisker inspired geometries as they apply to various engineering applications in drag reduction, vibration suppression, or hydrodynamic sensing. Although not explored here, future work could include active flow control techniques enabled through the mesh morphing algorithm.

5. Acknowledgement

The authors acknowledge Brown University's Center for Computation and Visualization for computational resources. Financial support is graciously provided by University of Wisconsin-Madison's Hilldale Undergraduate/Faculty Research Fellowship, Wisconsin Alumni Research Foundation's Fall Research Competition, and the National Science Foundation Award 2035789. Thank you to Kirby Heck and Trevor Dunt for suggestions to the manuscript.

References

[1] C. C. Ginter, F. E. Fish, C. D. Marshall, Morphological analysis of the bumpy profile of phocid vibrissae, Marine Mammal Science 26 (3) (2010) 733–743. doi:10.1111/j.1748-7692.2009.00365.x.

[2] W. Hanke, M. Witte, L. Miersch, M. Brede, J. Oeffner, M. Michael, F. Hanke, A. Leder, G. Dehnhardt, Harbor seal vibrissa morphology suppresses vortex-induced vibrations, Journal of Experimental Biology 213 (15) (2010) 2665–2672. doi:10.1242/jeb.043216.

[3] M. Witte, W. Hanke, S. Wieskotten, L. Miersch, M. Brede, G. Dehnhardt, A. Leder, On the wake flow dynamics behind harbor seal vibrissae – a fluid mechanical explanation for an extraordinary capability,

in: C. Tropea, H. Bleckmann (Eds.), Nature-Inspired Fluid Mechanics: Results of the DFG Priority Programme 1207 "Nature-inspired Fluid Mechanics" 2006-2012, Notes on Numerical Fluid Mechanics and Multidisciplinary Design, Springer Berlin Heidelberg, Berlin, Heidelberg, 2012, pp. 271–289. doi:10.1007/978-3-642-28302-4_17.

[4] H. Hans, J. Miao, G. Weymouth, M. Triantafyllou, Whisker-like geometries and their force reduction properties, in: 2013 MTS/IEEE OCEANS - Bergen, 2013, pp. 1–7.

[5] S. Wang, Y. Liu, Wake dynamics behind a seal-vibrissa-shaped cylinder: A comparative study by time-resolved particle velocimetry measurements, Experiments in Fluids 57 (3) (2016) 32. doi:10.1007/s00348-016-2117-9.

[6] K. Lyons, C. T. Murphy, J. A. Franck, Flow over seal whiskers: Importance of geometric features for force and frequency response, PLOS ONE 15 (10) (2020) 1–25. doi:10.1371/journal.pone.0241142.

[7] H. S. Yoon, S. H. Nam, M. I. Kim, Effect of the geometric features of the harbor seal vibrissa based biomimetic cylinder on the flow over a cylinder, Ocean Engineering 218 (2020) 108150. doi:10.1016/j.oceaneng.2020.108150.

[8] C. C. Ginter, T. J. DeWitt, F. E. Fish, C. D. Marshall, Fused traditional and geometric morphometrics demonstrate pinniped whisker diversity, PLOS ONE 7 (4) (2012) e34481. doi:10.1371/journal.pone.0034481.

[9] C. Murphy, Structure and function of pinniped vibrissae, Graduate Theses and Dissertations (Jan. 2013).

[10] A. Rinehart, V. Shyam, W. Zhang, Characterization of seal whisker morphology: Implications for whisker-inspired flow control applications, Bioinspiration & Biomimetics 12 (6) (2017) 066005. doi:10.1088/1748-3190/aa8885.

[11] G. Liu, Q. Xue, X. Zheng, Phase-difference on seal whisker surface induces hairpin vortices in the wake to suppress force oscillation, Bioinspiration & Biomimetics 14 (6) (2019) 066001. doi:10.1088/1748-3190/ab34fe.

[12] K. Lam, Y. F. Lin, Effects of wavelength and amplitude of a wavy cylinder in cross-flow at low Reynolds numbers, Journal of Fluid Mechanics 620 (2009) 195–220. doi:10.1017/S0022112008004217.

[13] M. L. Staten, S. J. Owen, S. M. Shontz, A. G. Salinger, T. S. Coffey, A comparison of mesh morphing methods for 3D shape optimization, in: W. R. Quadros (Ed.), Proceedings of the 20th International Meshing Roundtable, Springer, 2012, pp. 293–311. doi:10.1007/978-3-642-24734-7_16.

[14] J. A. Samareh, Survey of shape parameterization techniques for high-fidelity multidisciplinary shape optimization, AIAA Journal 39 (5) (2001) 877–884. arXiv:https://doi.org/10.2514/2.1391, doi:10.2514/2.1391.

[15] F. Gagliardi, K. C. Giannakoglou, RBF-based morphing of B-Rep models for use in aerodynamic shape optimization, Advances in Engineering Software 138 (2019) 102724. doi:https://doi.org/10.1016/j.advengsoft.2019.102724.

[16] D. Wei, S. M. J. Spence, A. Kareem, A. Jemcov, A structured mesh boundary motion approach for simulating wind effects on bluff bodies with changing boundaries, Journal of Wind Engineering and Industrial Aerodynamics 126 (2014) 118–131. doi:10.1016/j.jweia.2014.01.008.

[17] X. Yan, A. Mohammadian, C. D. Rennie, Numerical modeling of local scour due to submerged wall jets using a strict vertex-based, terrain conformal, moving-mesh technique in OpenFOAM, International Journal of Sediment Research 35 (3) (2020) 237 – 248. doi:https://doi.org/10.1016/j.ijsrc.2019.12.007.

[18] H. G. Weller, G. Tabor, H. Jasak, C. Fureby, A tensorial approach to computational continuum mechanics using object-oriented techniques, Computers in Physics 12 (6) (1998) 620–631, publisher: American Institute of Physics. doi:10.1063/1.168744.

[19] H. Jasak, Dynamic mesh handling in OpenFOAM, in: 47th AIAA Aerospace Sciences Meeting including The New Horizons Forum and Aerospace Exposition, Aerospace Sciences Meetings, American Institute of Aeronautics and Astronautics, 2009. doi:10.2514/6.2009-341.

[20] H. Kim, H. S. Yoon, Effect of the orientation of the harbor seal vibrissa based biomimetic cylinder on hydrodynamic forces and vortex induced frequency, AIP Advances 7 (10) (2017) 105015. doi:10.1063/1.5008658.

Appendix A. Appendix

Appendix A.1. Derivation of R_1 and R_2

An ellipse with radii a and b, can be expressed with the equation

$$\frac{x'^2}{a^2} + \frac{y'^2}{b^2} = 1 \tag{A.1}$$

in the coordinate system x', y' that has an angle α with respect to the x-axis.

In order to complete calculations parallel and perpendicular to the fluid flow, the coordinate system can be rotated about the y-axis using the transform

$$x = x' \cos\alpha \tag{A.2}$$

$$y = y'. \tag{A.3}$$

The ellipse is now represented in terms of x and y as

$$\frac{x^2}{a^2 \cos^2\alpha} + \frac{y^2}{b^2} = 1. \tag{A.4}$$

Next, substituting $y = x \tan\theta$, and solving for x, the ellipse equation can be rewritten in terms of θ as

$$x = \frac{ab\cos\alpha}{\sqrt{b^2 + (a\cos\alpha\tan\theta)^2}}. \tag{A.5}$$

Then, R_1 is defined by

$$R_1 = \sqrt{x^2 + y^2} = \frac{ab\cos\alpha}{\sqrt{(a\cos\alpha\sin\theta)^2 + (b\cos\theta)^2}}. \tag{A.6}$$

Using the same procedure, R_2 can be also derived as

$$R_2 = \frac{kl\cos\beta}{\sqrt{(k\cos\beta\sin\theta)^2 + (l\cos\theta)^2}}. \tag{A.7}$$